IEEE Access
Multidisciplinary | Rapid Review | Open Access Journal

Received June 22, 2021, accepted July 24, 2021, date of publication July 26, 2021, date of current version August 2, 2021.

Digital Object Identifier 10.1109/ACCESS.2021.3100505

An Automatic Method for Discontinuity Recognition in Coal-Measure Strata Borehole Images

SEN YANG, HONGRU LI, LI MA, AND WENYONG BAI
School of Energy Science and Engineering, Xi'an University of Science and Technology, Xi'an 710054, China
Corresponding author: Sen Yang (yangsen2009@outlook.com)

This work was supported by the National Natural Science Foundation of China under Grant 52004204.

ABSTRACT An automatic recognition of discontinuities in borehole images is a desirable way to overcome the inefficiency and inconsistency inherent in the conventional method of manual annotation. The rough borehole walls and prominent noise failed the application of existing recognition methods to borehole images taken in the coal-measure strata. This paper presents a novel approach to automatically convert coal-measure strata borehole images into identified discontinuity maps. The developed procedure formed an integrated feature representation for the borehole image through combining the color information of image and the textural features generated from multi-channel filtering. Image regions containing discontinuities are then separated from other regions by implementing fuzzy c-means clustering on the acquired feature representation. The identification of discontinuities is finally accomplished by searching for four predefined patterns (named topographic model) on the intensity transection of image regions. The proposed method is proven to be superior in the respects of noise suppression, discontinuity positioning, and recognition completeness.

INDEX TERMS Automatic recognition, borehole image, coal-measure strata, rock discontinuity.

I. INTRODUCTION

Coal-measure rock strata are commonly embedded discontinuities such as joints, beddings, fractures and interlayers. This inherent feature endows the rock mass with a variable nature. The spatial geometry and mechanical property of discontinuities is therefore fundamental to reconstruct the structural setting of the rock mass [1], [2]. The accuracy of this reconstruction determines the validity of the prediction of the mechanical and hydraulical behaviors of rock masses, which means the success or failure in many rock engineering projects such as ground support design, surface subsidence control, and coalmine water drainage.

The feasible *in situ* observations of rock mass discontinuities include rock core examination and borehole logging and imaging. From the accuracy perspective, the rock coring and channeling can disturb the natural structure of the rock strata. This leads to an inevitable data loss for discontinuity property hindering the evaluations of orientation, openness, and filling [3], [4]. In comparison, the borehole logging and imaging can provide the geometry and distribution of discontinuities through direct and *in situ* borehole observation. With the advantages of adaptability and efficiency, this technique has been extensively applied to the survey of underground rock structure [5], [6]. The pioneer borehole imaging apparatus was developed and instrumented in 1960s [7]. From then on, the digital image and panoramic imaging technologies have been continuously evolved and improved. As a result, the digital panoramic borehole imaging technique emerges. This technique can photograph the annular borehole wall and recording the features in a two-dimensional (2D) (or unrolled) image. The continuous record of borehole walls provides large volumes of raw data for the quantitative discontinuity measurements and statistics. The most important priority of data processing is the accuracy and efficiency of discontinuity recognition. However, the conventional manual annotation of borehole images suffers from three apparent weaknesses including: (1) inefficiency associated with high labor intensity and time consumption, (2) inconsistency of results between different operators and even the same operator for different times; (3) requirements of the professional experience and knowledge from operators.

The associate editor coordinating the review of this manuscript and approving it for publication was Geng-Ming Jiang.

The automation of discontinuity recognition is essential for not only the enhancement of efficiency but also the improvement of consistency and accuracy. The early methods for the automatic recognition of discontinuities formed a two-step framework consisted of image segmentation and discontinuity identification [7]–[9]. The image segmentation commonly adopts the thresholding method (or an edge detector) to compute an edge map, and then the discontinuity identification scans for sinusoids on the map by using the Hough transform (HT). Scholars in this field followed the two-step convention and kept working on the automated discontinuity recognition. The progress in this field is listed in Table 1. For the image segmentation improvement, Van Ginkel *et al.* (2001) [10] proposed an orientation space transform (OST) to include local orientation information of the original 2D image into the edge map, which was intended to enhance the capability of HT to recognize intersecting discontinuities. The authors acknowledged that many bad HT local maxima were still presented after adopting OST, therefore the anti-noise performance of OST is not the ultimate solution for image segmentation. Assous *et al.* (2014) [11] used a gradient-based edge detector (originally proposed by Lindeberg 1998 [12]) to obtain a preliminary edge map and refined it by using phase congruency (PC). They claimed that the algorithm was computationally efficient and returned a false positive rate between 2% and 5% for resistivity images. Al-Sit *et al.* (2015) [13] combined a modified Canny detector with the vector quantization network (VQN) clustering to prepare a prior classification of image segments for establishment of edge maps. The VQN clustering differentiated image segments in accordance with textural features generated by the Gabor filter. The authors claimed a better recognition rate than it of Assous *et al.* (2014) [11] and moderate computational efficiency. Ge *et al.* (2019) [14] adopted a similar procedure to take textural features as the benchmark for the prior classification of image segments. The textural features were calculated by using the gray-level co-occurrence matrix (GLCM) instead of the Gabor filter. Ge *et al.* (2019) [14] claimed that this method produced a better recognition than it of Wang *et al.* (2017) [15] and made high computational efficiency. As for the discontinuity location part, Chai *et al.* (2009) [16] employed discriminant function analysis (DFA) to recognize discontinuities from resistivity images. This process was established on a classification of GLCM features. Wu *et al.* (2011) [17] used a modified HT developed by Zou and Shi (2002) [18] to search for sinusoids on the edge map prepared by the thresholding and morphological operations (MO). This modified HT reduces computational power by decomposing the searching problem from 3D to 2D.

The aforementioned techniques primarily focused on the improvement of either image segmentation or discontinuity identification. Recently, Wang *et al.* (2017) [15] proposed a new pathway for improvement of both. They developed a gradient-based index and used it to detect image segments containing discontinuities, and then performed a customized fitting procedure on the well-segmented images to locate sinusoids representing discontinuities. The authors acknowledged the algorithm easily generated flawed results from the recognitions of intersected, filled, and incomplete discontinuities. In summary, most of the above techniques and algorithms were tested on borehole images (commonly taken

TABLE 1. A summary of existing methods for discontinuity recognition from borehole images.

Method	Image segmentation part	Discontinuity identification part	Parameters require manual adjustment
Hall et al. (1996) [7]	Thresholding and a customized edge detector	HT	Threshold value and criteria for HT peak
Thapa et al. (1997) [8]	Thresholding with a fixed value	HT	Criteria for HT peak
Glossop et al. (1999) [9]	Laplacian-of-Gaussian (LoG) detector	HT	Threshold of LoG detector and criteria for HT peak
Van Ginkel et al. (2001) [10]	OST	HT and post-processing	Parameters of orientation selective template filter and criteria for HT peak
Chai et al. (2009) [16]	Thresholding and MO	DFA and GLCM features	Threshold value, shape and size of MO element, and size of sampling window for GLCM calculations
Wu et al. (2011) [17]	Thresholding and MO	Modified HT	Threshold value, shape and size of MO element, size of searching window for baseline location, and criteria for HT peak
Assous et al. (2014) [11]	Lindeberg method, PC validation, and post-processing	Modified HT	Scale range of Lindeberg method, criteria for edge linking and removal, parameters for filter construction in PC, size of searching window for baseline location, and criteria for HT peak
Al-Sit et al. (2015) [13]	Gabor filter, VQN clustering, and modified Canny detector	Modified HT	Examples for VQN training, number of epochs for VQN training, thresholds of Canny detector, standard deviation of Gaussian filter, and criteria for HT peak
Wang et al. (2017) [15]	Local thresholding using a gradient-based index and post-processing	Sinusoid fitting	Criteria for region merging in post-processing, size of iteration step of sinusoid fitting, and criteria for the selection of fitted sinusoids
Ge et al. (2019) [14]	GLCM features, Canny detector, and post-processing	Sinusoid fitting	Size of sampling window for GLCM calculations, thresholds of Canny detector, standard deviation of Gaussian filter, and criteria for the selection of edges

in clear drilling fluid) with well-defined discontinuities and a low level of noise. These images are vastly different from the images acquired in the coal-measure strata boreholes, which are featured by poor illumination and rough borehole walls as illustrated in Figure 1. The robustness of these methods is challenging in the discontinuity recognition of coal-measure strata borehole images. Moreover, a tendency can also be observed from the right column of Table 1 suggesting the subjective results due to the increase of parameters requiring manual adjustments. These parameters are an inconvenience in the creation of an automatic recognition tool. In this study, we initially analyzed the underlying mechanisms of the poor quality of coal measure strata borehole images. Then we proposed an improved method for discontinuity recognition and the new method were validated through a series of experiments. This study offers a robust approach to automatically identify the discontinuity of the coal-measure strata, which are paramount for the ground control design and optimization.

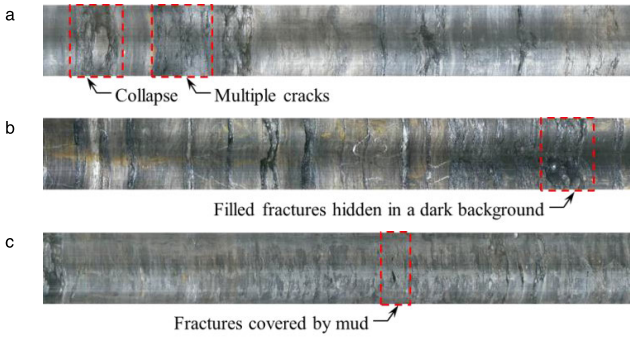

FIGURE 1. Borehole images of coal-measure strata acquired from coal mines located at: (a) Pingliang, gansu province, (b) and (c) Yangquan, shanxi province.

II. BOREHOLE IMAGES OF COAL-MEASURE STRATA

Three borehole images with each one recording 3.3-meter length were exhibited in Figure 1. They were photographed at two underground coal mines in China by using a panoramic-optical probe (manufactured by Wuhan Changsheng Coalmine Safety Technology CO., Ltd, Wuhan, China). The horizontal and vertical resolutions are 0.1 and 0.2 mm, respectively. Figure 1 illustrates that the coal-measure discontinuities are apparently different from ideal planar feature due to some inherent properties of coal-measure rocks.

First, the drilling-induced unevenness of borehole images can be resulted from borehole wall failure. The intersection of a discontinuity and the borehole is vulnerable for damage during drilling because the coal-measure strata commonly consist of weak rocks such as shale, siltstone and mudstone (Das, 2000 [19]; Wang *et al.*, 2019 [20]). From Figure 1a, a drilling-induced collapse of the intersection can be observed and it naturally alters the geometry of discontinuity displayed on the image, which is initially believed to be a sinusoid. Furthermore, the development of a discontinuity tends to form an aligned crack group in the weak stratum, which can result in multiple cracks occurring on a narrow region (Figure 1a). These irregularities apparently violate the sinusoid assumption of previously proposed methods discussed in the literatures. Second, discontinuities can be easily hidden in a noisy background for their recognition and identification. The coal-measure rocks are commonly rich in dark/dull bands due to the organic-bearing strata and therefore the borehole wall of coal measure strata is expected to be a dark hue. Unfortunately, the discontinuities are identified as a dark visible curve compared to its solid rock counterparts. Undoubtedly, the contrast between dark discontinuity and the coal measure rock strata are significantly small compared to other rock strata, which results in that the chance of misidentification of discontinuities is much higher. Nonetheless, the uneven illumination and the fillings of discontinuity complicate the discontinuities recognition. As an example, the windowed area shows three fractures being filled with dark minerals and is overlapped with a stripe-shaped shadow in Figure 1b. These adverse factors blur the boundary between discontinuities and the dark solid wall. Third, the shale and mudstone are known to be water-sensitive, thus the drilling operation easily generates a large volume of fine slurry. The slurry can form a drilling cake for patching the discontinuities and thus the image cannot capture the discontinuity. The windowed area of Figure 1c shows the adverse effects of mud to the imaging of discontinuities.

These three limitations necessitate a careful evaluation of the information included in coal-measure strata borehole images. The previously discussed methods in the introduction section commonly begin with conversions of images from the true color to the grayscale intensities. This can cause an irreversible loss of color information. As a result, the recognition of discontinuities relies solely on a detection of the gradient of pixel intensity. This procedure was referred to as the ''crude segmentation'' by Van Ginkel *et al.* (2001) [10] and Assous *et al.* (2014) [11], and its failure of the discontinuity recognition in a noisy environment was confirmed. Therefore, we proposed our automatic method for discontinuity recognition and identification.

III. PROPOSED METHOD FOR AUTOMATIC RECOGNITION OF COAL-MEASURE BOREHOLE IMAGES

The proposed automatic method for discontinuity recognition based on the coal-measure borehole images includes three major steps and is illustrated in Figure 2. We elaborated the detailed procedure for the method and all required parameters are defined and specified in order to eliminate the obstacles to automation. The detailed procedure and underly algorithms were discussed in the subsequent sections.

A. EXTRACTION OF TEXTURAL FEATURES

The concept of the texture of image data is based on the spatial distribution of tonal variations within a band (Haralick *et al.*, 1973 [21]). Mining engineers naturally use the textural features in interpreting borehole images and discriminating

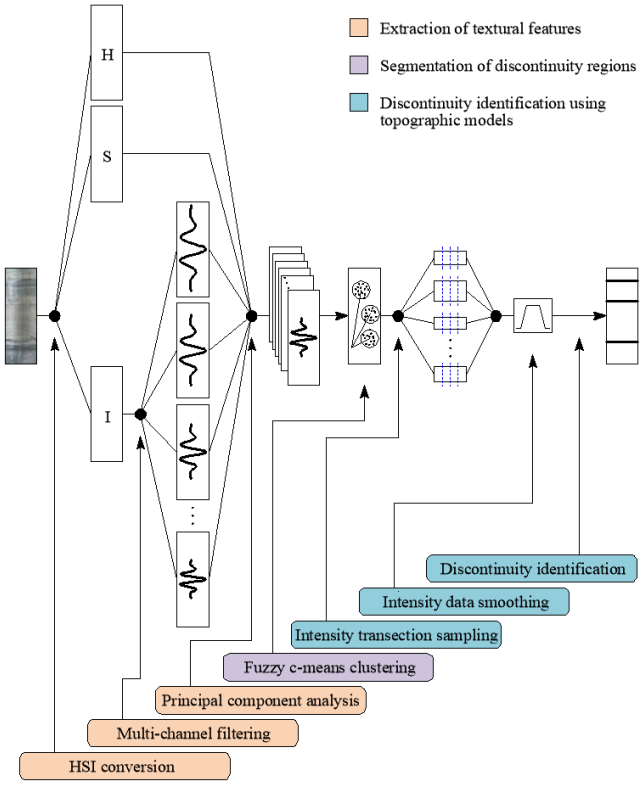

FIGURE 2. **Flow chart of the discontinuity recognition (H, S, and I indicate the hue, saturation, and intensity components of borehole images, respectively).**

discontinuities from rock matrices. For the automation of discontinuity recognition, a meaningful textural feature is of primary importance for the clustering of image regions which is the segmentation approach adopted in Section IIIB. In this study, the multi-channel filtering technique (Saeedi *et al.*, 2010 [22]) is adopted to extract textural features from the coal-measure strata borehole images. This technique enables a multi-resolution examination of differences in dominant sizes and orientations of different textures. This advantage is appealing because the rock discontinuity is characterized by the variation of size and geometry.

In our proposed method, the multi-channel filtering was achieved by applying a set of real-valued, even-symmetric Gabor filters (Jain and Farrokhnia, 1991 [23]) to the intensity component of borehole images. These Gabor filters are the representation of channels and can be understood as an approximate basis for a wavelet transform, with the Gabor function (given in (1)) as the wavelet.

$$IR(x, y) = \exp\left\{-\frac{1}{2}\left[\frac{x^2}{\sigma_x^2} + \frac{y^2}{\sigma_y^2}\right]\right\}\cos(2\pi ux) \tag{1}$$

here,

$$\sigma_x = \frac{1}{\pi}\sqrt{\frac{\ln 2}{2}}\cdot\frac{2^{b_u}+1}{2^{b_u}-1}\cdot\frac{1}{u} \tag{2}$$

$$\sigma_y = \frac{1}{\pi}\sqrt{\frac{\ln 2}{2}}\cdot\left(\tan\frac{b_\alpha}{2}\right)^{-1}\cdot\frac{1}{u} \tag{3}$$

where IR is the impulse response of an even-symmetric Gabor filter, u is the frequency of a sinusoidal plane wave along the x-axis (*i.e.* the 0° orientation) and expressed in cycles per image-width, σ_x and σ_y are the space constants of the Gaussian envelope along the x and y axes, respectively. Filters with an arbitrary orientation α (in degrees) can be obtained through rotating the x-y coordinate system by the angle α. b_u (in octaves) and b_α (in degrees) denote the bandwidths of the frequency and orientation of the Gabor filter set, respectively.

u, α, b_u, and b_α are the filter parameters need to be specified for automatic recognition. It is noted that the frequency bandwidth b_u is one octave apart, which means it is calculated by the following equation:

$$b_u = \log_2\left(u_{max}/u_{min}\right) \tag{4}$$

where u_{max} and u_{min} denote the maximum and minimum values of the frequency u. The values of u of the Gabor filter set were determined by the equation:

$$u_n = \frac{\sqrt{2}}{2^{C-n}}W, \quad n = 0, 1, 2, \ldots, C-2 \tag{5}$$

where W is the width of borehole images (in terms of pixel distance), C is a fixed parameter that is related to W by the formula:

$$2^C \geq W \;\&\; 2^{C-1} < W \tag{6}$$

Substitute (6) into (5), the maximum and minimum values of u can be derived as $\frac{\sqrt{2}}{4}W$ and $\frac{\sqrt{2}}{2^C}W$ cycles per image-width. The rationale behind the choices of these two values is two reasons. The first reason is that the highest frequency selected is the upper limit of Gabor filter set defined by Jain and Farrokhnia (1991) [23]. By setting this value, the fine variation of image texture can be captured. The second reason is that the selection of the lowest frequency was based on the assumption that the largest dimension of discontinuity-induced textural variation is of the same order as the image width. As for the orientation α of the Gabor filter set, four values were determined as 0°, 45°, 90°, 135°. Accordingly, the bandwidth of orientation b_α was calculated as 135°. Although a finer quantization of orientation is beneficial to the examination of texture, the four orientations are sufficient for detecting variations in the major directions (*i.e.* horizontal, vertical, and diagonal). More importantly, this restriction improved the computational efficiency of the recognition method presented in this study.

The efficiency of computation was also made by applying the multi-channel filtering to the shrunken borehole image. We used bicubic interpolation method (Carey *et al.*, 1999 [24]) to scale down the virgin image by a ratio of 0.25, which reduced the size from 6600×795 to 1650×199. In this study, the textural features were extracted from the intensity component of borehole images. The other two components (*i.e.* hue and saturation) served as two additional features in the subsequent image segmentation. This method allows us to incorporate true-color information (discussed in Section II)

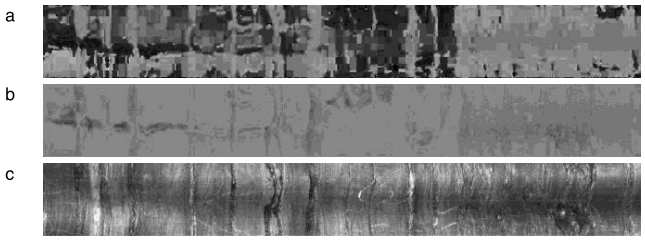

FIGURE 3. Hue, saturation, and intensity components calculated froms a borehole image: (a) hue, (b) saturation, (c) intensity.

into the clustering without lost of color-to-gray image conversion. Hue (H), saturation (S), and intensity (I) components were calculated from the RGB image in which each color pixel is a triplet corresponding to the red (R), green (G), and blue (B) components at a specific spatial location. The H, S, and I components of shrunken Figure 1b were presented in Figure 3 as an illustration. Conversion equations are:

$$H = \begin{cases} \theta & \text{if } B \le G \\ 360 - \theta & \text{if } B > G \end{cases} \tag{7}$$

with

$$\theta = \cos^{-1}\left\{ \frac{0.5\left[(R\text{-}G) + (R\text{-}B)\right]}{\left[(R-G)^2 + (R-B)(G-B)\right]^{1/2}} \right\} \tag{8}$$

$$S = 1 - \frac{3}{(R+G+B)}\left[\min(R, G, B)\right] \tag{9}$$

$$I = \frac{1}{3}(R+G+B) \tag{10}$$

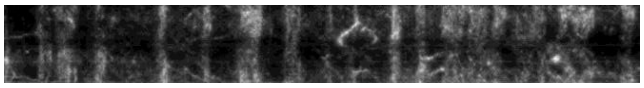

FIGURE 4. The feature image reconstructed by PCA.

Given the image width is 199 (in pixel distance), a total of 28 Gabor filters were used in the multi-channel filtering, resulting in 28 textural-feature images with the same dimension of the input image (1650 × 199). The 28 textural-feature and 2 color-feature images give a 30-dimensional representation of each pixel in the input image. The segmentation algorithm described in Section IIIB requires of an integration of this multi-dimensional representation into a 1-dimensional magnitude value for each pixel. Here, the principal component analysis method (PCA) is employed to achieve this integration. PCA generated a new group of variables from the original 30 variables of pixels. Each new variable will be a linear combination of the original variables. These new variables are orthogonal to each other and named principal components. Among them, the first principal component was selected to reconstruct a single-feature image shown in Figure 4. The first principal component was seen as a single axis in the multi-dimensional space. When projecting each data point on this axis, the resulting values form a new variable. And the variance of this variable is the maximum among all possible choices of the first axis. This definition indicates that the feature image in Figure 4 captured the largest variation of data in the above-mentioned 30-dimensional representation. Detailed descriptions of the PCA can be found in several publications (*e.g.* Wold *et al.*, 1987 [25]; Abdi and Williams, 2010 [26]).

B. SEGMENTATION OF DISCONTINUITY REGIONS

The image segmentation is to locate the exact regions containing discontinuities, which is a guarantee of the accuracy of subsequent identification of discontinuity. The fuzzy c-means clustering method (FCM) was adopted to separate these candidate regions from the intact rock-wall regions. FCM is implemented through minimizing the following objective function (Bezdek JC, 1981 [27]):

$$J_m = \sum_{i=1}^{a}\sum_{j=1}^{c} {p_{ij}}^m d^2\left(x_i, e_j\right) \tag{11}$$

where a is the number of data points, c is the number of clusters, here, c was fixed as 2, which means the borehole image was divided into two groups of regions with one group representing discontinuities and the other representing intact rock wall. m is the degree of fuzzy overlap between clusters and is a real number greater than 1, x_i denotes the ith data point, e_j is the center of the jth cluster, $d^2(x_i, e_j)$ denotes the distance between x_i and e_j, p_{ij} is the degree of membership of x_i in the jth cluster. Given a data point, x_i, the sum of the membership values for all clusters is one.

FCM enables us to evaluate the belonging of data points having maximum membership values below 0.6, because these points possess a high degree of uncertainty in their cluster membership. In our proposed method, the cluster of candidate discontinuities was formed by including the data points with membership values to it greater than 0.4. This procedure was intended to increase the likelihood of containing all image regions holding the discontinuity. If the regions are lost in this step, they cannot be recovered in the subsequent procedures. The overall process is specified as the following steps: first, we represented each column of pixels in Figure 4 with five statistical parameters including arithmetic mean, median, standard deviation, maximum, and minimum values. And then the dataset was prepared by setting pixel columns as data points and the five parameters as variables representing a five-dimensional space in which $d^2(x_i, e_j)$ are calculated. This step indicates that the image segmentation is realized by clustering the pixel columns in borehole images; second, we added the spatial sequence of the pixel columns (*i.e.* 1, 2, 3, . . .) to the dataset as the sixth dimensionality. This step encourages neighboring columns to cluster together; third, the cluster membership values, p_{ij} is randomly initialized; fourth, the centers of clusters were calculated by using:

$$e_j = \frac{\sum_{i=1}^{a} p_{ij}^m x_i}{\sum_{i=1}^{a} p_{ij}^m} \tag{12}$$

fifth, we re-calculated the memberships according to (13):

$$p_{ij} = \frac{1}{\sum_{k=1}^{c} \left[\frac{d^2(x_i, e_j)}{d^2(x_i, e_k)} \right]^{\frac{1}{m-1}}} \tag{13}$$

sixth, the objective function, J_m was updated; finally, we repeated steps 4 to 6 until J_m improves by less than 1×10^{-5}. Figure 5 shows the obtained result from the image segmentation. The regions of rock wall were labeled with mesh-cover, while the regions of discontinuity remained unchanged.

FIGURE 5. The result of image segmentation.

C. DISCONTINUITY IDENTIFICATION USING TOPOGRAPHIC MODELS

From Figure 5, it is apparent that the discontinuity regions were well segmented. The next work is to identify discontinuities from each region and form a trace map that is of practical values to the mining and geotechnical engineering. Instead of making use of a gradient-based edge detector like the methods listed in Table 1 did (reasons are discussed in Section IV), we developed a method to pick out discontinuities through recognizing typical patterns in the intensity transection of regions. This process includes the following three steps:

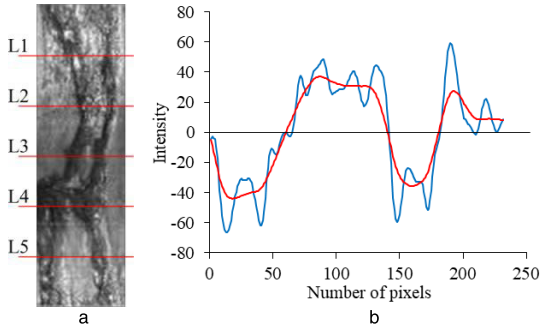

FIGURE 6. Illustration of the sampling of intensity transections: (a) layout of sampling lines, (b) processed data of the intensity transection along L5 (the blue curve indicates the intensity transection along L5; the red curve shows the result of filtering).

First, the intensity transections of discontinuity regions were sampled. The image region in Figure 6a is taken as an example to illustrate the procedure. This region is a segment of the intensity component of the virgin borehole image (*viz.* the image has not been shrunken in Section IIIA). It was located by substituting the numbers of leftmost and rightmost pixel columns of a segmented region of Figure 5 into (14) and (15), respectively. As shown in Figure 6a, the sampling lines were evenly spaced and therefore the spacing can be calculated as 132 (in pixel distance). The sampling rate (or spacing) can be customized in order to satisfy different engineering purposes. The blue curve in Figure 6b is the result of the intensity transection along L5 subtracted its mean.

$$N_l' = N_l \times 4 - 3 \tag{14}$$

$$N_r' = N_r \times 4 \tag{15}$$

where the N_l' and N_r' are the numbers of leftmost and rightmost pixel columns of regions in the virgin borehole image. N_l and N_r are the corresponding column numbers of regions in the shrunken borehole image.

Second, the intensity data was smoothed by using zero-phase moving-average filtering (ZMF). ZMF is developed from the moving-average filtering (MAF) which calculates a local mean value for each element of input data. Each mean is derived by averaging neighboring elements within a sliding window of length h. ZMF reduces the phase distortion through performing MAF in both forward and backward direction, *i.e.* filter the input data, then reverse the data array and filter again, and then reverse again. The detailed descriptions of ZMF and MAF can be found in Mitra (2001) [28]. The red curve in Figure 6b is the result derived from applying ZMF to the data shown in the blue curve. It can be observed that ZMF filtered the high-frequency component of input data and therefore reduced the number of zero-crossings from seven to three. The zero-crossing is the most important feature used in the next step to identify discontinuities. Another benefit from ZMF is the preservation of the spatial-domain features of input data, to be specific, the red curve shows no clear horizontal shift to the blue curve, which is a guarantee for the accuracy of the location of discontinuities. The length of sliding window, h, was set as the one-twelfth of the total number of pixel columns (for a decimal, round it toward negative infinity) in the image region under consideration.

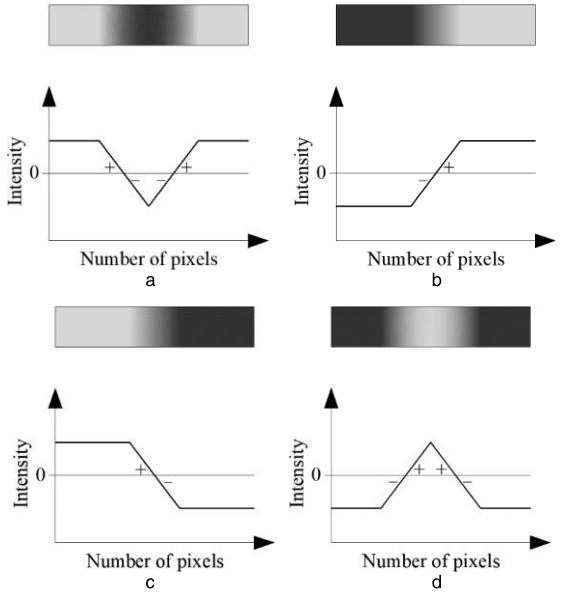

FIGURE 7. Four topographic models corresponding to different discontinuities: (a) a ravine, (b) an up-ramp, (c) a down-ramp, (d) a peak.

Third, discontinuities were identified by using topographic models. Four models for the intensity transection of image region were developed and illustrated in Figure 7. Each model

represents a type of discontinuity trace shown on the borehole image. Figure 7a is the typical pattern for fractures, cracks, and separation of layers. Their intensity transections are characterized with a low middle and two high sides, which can be likened to a ''ravine''. There are two zero-crossings in this model, and the change of sign starts from positive to negative and then back to positive. Figure 7b and c are the representation of the boundary of layers, which involves a transition between two intensity levels. This model is named as ''ramp'' and has one zero-crossing from negative to positive and vice versa. The model in Figure 7d is commonly seen at discontinuities filled with reflective minerals or other interlayers. The curve of intensity transection is featured by a ''peak'' shape, and has two zero-crossings involving a transition from negative to positive and back to negative. Use the model in Figure 7 to recognize discontinuities in each intensity transection (after the smoothing process), and the priority is: the ravine after by the ramp, and then the peak. This sequence was determined based on the fact that the separation of layers and beddings are the most prevailing discontinuity in coal-measure formation. For example, a ravine type can be found at the right side of red curve in Figure 6b, while a ramp type is observed at the left side. The exact location of discontinuity is calculated as the location corresponding to the highest or lowest intensity value for the ravine or peak type, to the zero-crossing for the ramp type. Figure 8 presents the discontinuity traces (in yellow) identified from the image region shown in Figure 6a.

FIGURE 8. Identified discontinuity traces (in yellow) by using the topographic model.

IV. EXPERIMENTAL RESULTS AND DISCUSSION

An evaluation of the performance of our proposed method was conducted with reference to the three borehole images in Figure 1. Figure 9-11 shows the experimental results produced by the proposed method and other three previous methods—Assous *et al.* (2014) [11], Al-Sit *et al.* (2015) [13], and Ge *et al.* (2019) [14] (see Table 1). As described in Section I, the previous methods postulated a planar feature for discontinuities, and therefore included a step of sinusoid searching. Since this assumption was invalidated by the geometrical irregularities of discontinuities as explained in Section II, we discarded the sinusoid searching step and presented the results generated from the image segmentation

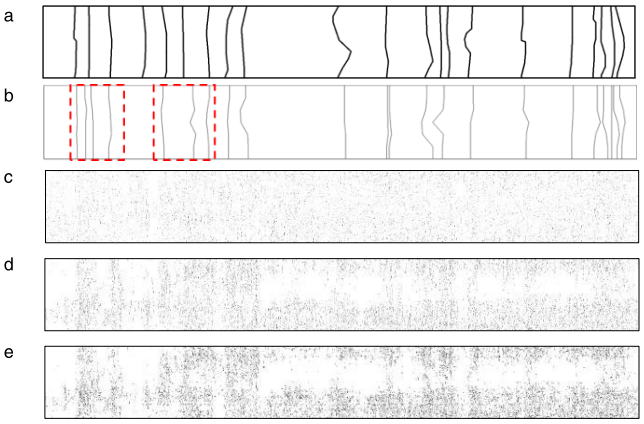

FIGURE 9. Results generated from the borehole image acquired at pingliang, gansu province by using different recognition methods: (a) manual tracing, (b) the proposed method (the dotted frames show the collapse and multiple cracks, respectively), (c) Assous *et al.* (2014) [11], (d) Al-Sit *et al.* (2015) [13], and (e) Ge *et al.* (2019) [14].

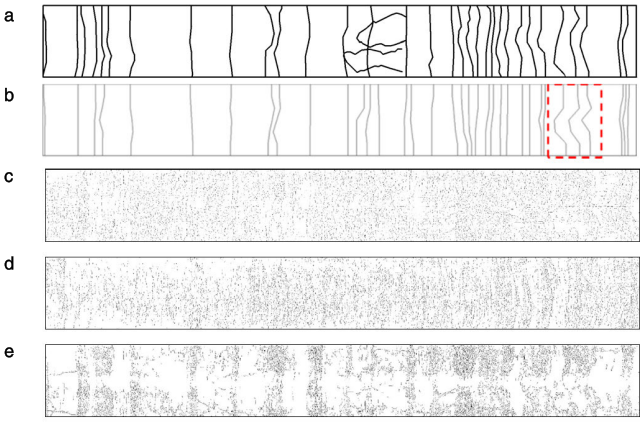

FIGURE 10. Results generated from the borehole image acquired at yangquan, shanxi province by using different recognition methods: (a) manual tracing, (b) the proposed method (the dotted frame shows the dark area), (c) Assous *et al.* (2014) [11], (d) Al-Sit *et al.* (2015) [13], and (e) Ge *et al.* (2019) [14].

part of the previous methods. The parameters of them (as listed in Table 1) are manually adjusted in order to reach the optimal result. The experiments were carried out on a standard personal laptop with an Intel Core i7 CPU running at 2.3GHz and an 8.00 GB RAM. The computational time for the proposed method was 32 s for 3.3 m of 0.1 mm sampled data. This computational efficiency can be improved by using parallel computing techniques. Due to the interruptions of manual adjustments, the computational time of other previous methods was hardly recorded. Furthermore, at the top of each figure, a hand-drawn discontinuity trace map was supplemented as a benchmark for the performance assessment of our proposed method as well as the previous methods. A geologist was invited to prepare these trace maps by using a printed copy of the borehole image, a sheet of transparent tracing paper, and a pen. He worked independently and no other instructions were given. The obtained trace maps were then digitized and exhibited in Figure 9a-11a.

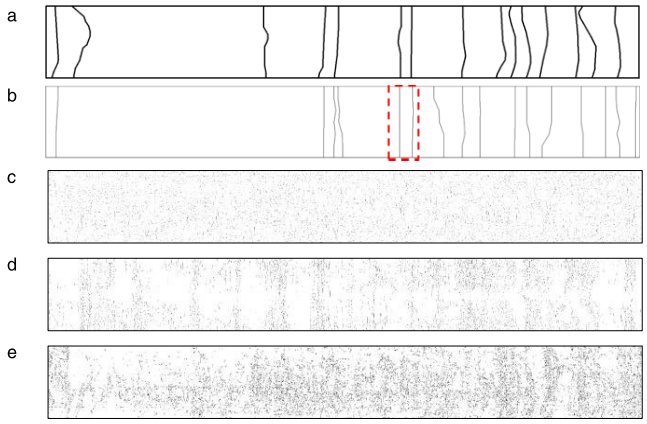

FIGURE 11. Results generated from the borehole image acquired at yangquan, shanxi province by using different recognition methods: (a) manual tracing, (b) the proposed method (the dotted frame shows the mud-covered area), (c) Assous *et al.* (2014) [11], (d) Al-Sit *et al.* (2015) [13], and (e) Ge *et al.* (2019) [14].

Through a comparison between the results of previous methods (Figure 9c d e-11c d e) and manual tracing (Figure 9a-11a), it can be observed that the erroneous responses dominate the edge maps of previous methods. These noises hindered the attempt to determine whether a discontinuity was recognized as a corresponding edge or the edge was just a random noise. Therefore, the quantitative characterization of the performance of previous methods was hardly realized. Another obvious feature of the edge maps of previous methods is the incompleteness of edges. This incompleteness can be attributed to two reasons: (1) uneven illumination and (2) rough borehole walls. As mentioned in Section II, the uneven illumination commonly interferes the imaging of borehole walls, leaving stripe-shaped shadows at the center or the sides of images (see Figure 1). The presence of shadow would dramatically deteriorate the performance of a gradient-based edge detector like the canny detector adopted in Al-Sit *et al.* (2015) [13] and Ge *et al.* (2019) [14] (see Table 1), and thus leads to the loss of edge information at the corresponding location as shown in Figure 9d e-11d e. For edge maps of Assous *et al.* (2014) [11] (Figure 9c-11c), the effect of shadow was greatly weakened, but the edges were broken into a high number of small curve segments, which is a result of the poor image contrast induced by rough borehole walls. The exposed problems of incompleteness of recognition and erroneous responses are consistent with the findings of a previous evaluation test (Yang *et al.* 2021 [29]) on gradient-based edge detectors to rock discontinuity recognition.

TABLE 2. Performance of the proposed method for the investigated images. (unit: %).

No. of images	1	2	3	Average values
Recognition rate	90.5	91.2	73.3	85.0
Error rate	13.6	11.4	31.3	18.8

The detected discontinuities of our proposed method are shown in Figure 9b-11b. Apparently, these results demonstrate a superior performance of the proposed method for noise suppression, discontinuity positioning, and recognition completeness. The trace maps produced by the method and the manual drawing are matched to a relatively high degree. This indicates that the proposed method overcame the adverse conditions described in Section II and yielded quite satisfactory results for various types of discontinuities including filled and unfilled fractures, cracks, beddings, interlayers, *etc*. More notably, the discontinuities identified in dashed boxes of Figure 9b-11b can be one-to-one corresponding to discontinuities traced in Figure 9a-11a. These dashed boxes covered the areas of rough cuts, uneven illumination, and mud contamination shown in Figure 1a b c, therefore, these results of recognition demonstrate that the adaptability of the proposed method to the coal-measure environment is as good as it of the manual tracing. It should be also noted in this comparison that the digitized traces of manual drawing are not recognized objects representing discontinuities but pixel aggregates need further processing before they can be utilized for the automated computation of discontinuity parameters. For results generated by the proposed method, this problem is untroubled, since the image coordinates of all pixels constituting a particular discontinuity are obtained and can be directly used for an automated computation.

A quantitative evaluation of the performance of the proposed method was conducted based on two criteria—recognition and error rates (RR and ER) and the results are summarized in Table 2. The two rates are defined as (16) and (17), as shown at the bottom of the page.

In Table 2, the No. 1 2 3 images refer to Figure 1a b c, respectively. It can be seen that the average RR is as high as 85.0 % but the average ER is unsatisfactorily equal to 18.8 %. This moderately high value of ER is obviously a result of the high value of ER attained in the recognition of No. 3 image. The RR of No. 3 image is also lower than it of either No. 1 or 2 images. The high ER and low RR demonstrate that, compared with rough cuts and uneven illumination,

$$\mathrm{RR} = \frac{\sum(\text{detected discontinuities matched with manual traces})}{\sum(\text{discontinuities traced by manual drawing})} \times 100\% \tag{16}$$

$$\mathrm{ER} = \frac{\sum(\text{detected discontinuities not matched with manual traces})}{\sum(\text{discontinuities traced by manual drawing})} \times 100 \tag{17}$$

the interference of drilling mud posed a stronger deteriorating effect to the performance of the method.

Although the RR of 73.3 % is acceptable, further improvement of the proposed method is considering establishing a preprocessing procedure for borehole images in order to minimize the contamination of drilling mud. Ongoing research also intends to conduct a comprehensive evaluation test on the robustness of the proposed method to various kinds of geological environments, especially to water-filled boreholes in petroleum engineering and high-temperature formations in geothermal engineering.

V. SUMMARY AND CONCLUSION

A novel method for the automatic recognition of discontinuities from borehole images taken in coal-measure strata is presented. A series of algorithms were designed to overcome the disadvantages of imaging conditions in the borehole. The robustness and accuracy of the proposed method are validated by several experimental tests. Based on results, the following conclusions can be drawn:

(1) The combined effect of drilling disturbance and weak rock strength distorted the geometry of discontinuities shown on the coal-measure strata borehole image, and therefore invalidated the sinusoid assumption of ideal planar feature. Furthermore, the image degradation from uneven illumination and mud contamination complicated the already challenging problem of recognition.

(2) The proposed method is superior in the respects of noise suppression, discontinuity positioning, and recognition completeness. Under the adverse conditions of coal-measure strata borehole imaging, this method was able to detect various types of discontinuities including filled and unfilled fractures, cracks, beddings, interlayers, etc.

(3) The incorporation of textural features and color information into the segmentation of discontinuity region gave rise to an accurate positioning of discontinuity in noisy borehole images.

(4) The concept of considering an intensity transection of the image region as a 1-dimentional representation of the variation tendency in elevation, and then identifying discontinuities through searching for four predefined patterns (named topographic model) was shown to be valid for the coal-measure strata borehole images.

REFERENCES

[1] L. Fan and S. Liu, "Numerical prediction of *in situ* horizontal stress evolution in coalbed methane reservoirs by considering both poroelastic and sorption induced strain effects," *Int. J. Rock Mech. Mining Sci.*, vol. 104, pp. 156–164, Apr. 2018.

[2] M. Brook, B. Hebblewhite, and R. Mitra, "Coal mine roof rating (CMRR), rock mass rating (RMR) and strata control: Carborough Downs mine, Bowen basin, Australia," *Int. J. Mining Sci. Technol.*, vol. 30, no. 2, pp. 225–234, Mar. 2020.

[3] T. Malone, B. Hubbard, D. Merton-Lyn, P. Worthington, and R. Zwiggelaar, "Borehole and ice feature annotation tool (BIFAT): A program for the automatic and manual annotation of glacier borehole images," *Comput. Geosci.*, vol. 51, pp. 381–389, Feb. 2013.

[4] X. Zou, C. Wang, Y. Wang, and H. Song, "Morphological feature description method of structural surface in borehole image during *in-situ* instrumentation," *Rock Mech. Rock Eng.*, vol. 53, no. 7, pp. 2947–2956, Mar. 2020.

[5] H. Zhang, H. Li, D. Lu, and Y. Xie, "An improved LWD azimuth gamma imaging model based on HSI space," *IEEE Access*, vol. 8, pp. 112160–112169, Jun. 2020.

[6] Z. Han, C. Wang, C. Wang, X. Zou, Y. Jiao, and S. Hu, "A proposed method for determining *in-situ* stress from borehole breakout based on borehole stereo-pair imaging technique," *Int. J. Rock Mech. Mining Sci.*, vol. 127, Mar. 2020, Art. no. 104215.

[7] J. Hall, M. Ponzi, M. Gonfalini, and G. Maletti, "Automatic extraction and characterisation of geological features and textures from borehole images and core photographs," in *Proc. Soc. Petrophysicists Well-Log Analysts 37th Annu. Logging Symp.*, New Orleans, LA, USA, 1996, pp. 1–13.

[8] B. B. Thapa, P. Hughett, and K. Karasaki, "Semi-automatic analysis of rock fracture orientations from borehole wall images," *Geophysics*, vol. 62, no. 1, pp. 129–137, Jan. 1997.

[9] K. Glossop, P. J. G. Lisboa, P. C. Russell, A. Siddans, and G. R. Jones, "An implementation of the Hough transformation for the identification and labelling of fixed period sinusoidal curves," *Comput. Vis. Image Understand.*, vol. 74, no. 1, pp. 96–100, Apr. 1999.

[10] M. Van Ginkel, M. A. Kraaijveld, L. J. Van Vliet, E. P. Reding, P. W. Verbeek, and H. J. Lammers, "Robust curve detection using a radon transform in orientation space applied to fracture detection in borehole images," in *Proc. 7th Annu. Conf. Adv. School Comput. Imag.*, Heijen, The Netherlands, 2001, pp. 84–91.

[11] S. Assous, P. Elkington, S. Clark, and J. Whetton, "Automated detection of planar geologic features in borehole images," *Geophysics*, vol. 79, no. 1, pp. D11–D19, Jan. 2014.

[12] T. Lindeberg, "Edge detection and ridge detection with automatic scale selection," *Int. J. Comput. Vis.*, vol. 30, no. 2, pp. 117–156, Sep. 1998.

[13] W. Al-Sit, W. Al-Nuaimy, M. Marelli, and A. Al-Ataby, "Visual texture for automated characterisation of geological features in borehole televiewer imagery," *J. Appl. Geophys.*, vol. 119, pp. 139–146, Aug. 2015.

[14] Y. Ge, P. Zhong, and H. M. Tang, "Intelligent measurement on geometric information of rock discontinuities based on borehole image," (in Chinese), *Rock Soil Mech.*, vol. 40, no. 11, pp. 4467–4476, Nov. 2019.

[15] C. Wang, X. Zou, Z. Han, J. Wang, and Y. Wang, "The automatic interpretation of structural plane parameters in borehole camera images from drilling engineering," *J. Petroleum Sci. Eng.*, vol. 154, pp. 417–424, Jun. 2017.

[16] H. Chai, N. Li, C. Xiao, X. Liu, D. Li, C. Wang, and D. Wu, "Automatic discrimination of sedimentary facies and lithologies in reef-bank reservoirs using borehole image logs," *Appl. Geophys.*, vol. 6, no. 1, pp. 17–29, Jan. 2009.

[17] J. Wu, S. Feng, and H. Li, "Study of automatically extracting structural plane parameters from borehole images," (in Chinese), *Rock Soil Mech.*, vol. 32, no. 3, pp. 951–957, Mar. 2011.

[18] Z. Changchun and S. Ge, "A Hough transform-based method for fast detection of fixed period sinusoidal curves in images," in *Proc. 6th Int. Conf. Signal Process.*, Beijing, China, 2002, pp. 909–912.

[19] S. K. Das, "Observations and classification of roof strata behaviour over longwall coal mining panels in India," *Int. J. Rock Mech. Mining Sci.*, vol. 37, no. 4, pp. 585–597, Jun. 2000.

[20] B. Wang, F. Dang, W. Chao, Y. Miao, J. Li, and F. Chen, "Surrounding rock deformation and stress evolution in pre-driven longwall recovery rooms at the end of mining stage," *Int. J. Coal Sci. Technol.*, vol. 6, no. 4, pp. 536–546, Nov. 2019.

[21] R. M. Haralick, K. Shanmugam, and I. Dinstein, "Textural features for image classification," *IEEE Trans. Syst., Man, Cybern.*, vol. SMC-3, no. 6, pp. 610–621, Nov. 1973.

[22] J. Saeedi, M. H. Moradi, and K. Faez, "A new wavelet-based fuzzy single and multi-channel image denoising," *Image Vis. Comput.*, vol. 28, no. 12, pp. 1611–1623, Dec. 2010.

[23] A. K. Jain and F. Farrokhnia, "Unsupervised texture segmentation using Gabor filters," *Pattern Recognit.*, vol. 24, no. 12, pp. 1167–1186, May 1991.

[24] W. K. Carey, D. B. Chuang, and S. S. Hemami, "Regularity-preserving image interpolation," *IEEE Trans. Image Process.*, vol. 8, no. 9, pp. 1293–1297, Sep. 1999.

[25] S. Wold, K. Esbensen, and P. Geladi, "Principal component analysis," *Chemometrics Intell. Lab. Syst.*, vol. 2, nos. 1–3, pp. 37–52, Aug. 1987.

[26] H. Abdi and L. J. Williams, "Principal component analysis," *Wiley Interdiscipl. Rev., Comput. Statist.*, vol. 2, no. 4, pp. 433–459, Jul. 2010.

[27] J. C. Bezdek, *Pattern Recognition With Fuzzy Objective Function Algorithms*. New York, NY, USA: Plenum Press, 1981.

[28] S. K. Mitra, *Digital Signal Processing*, 2nd ed. New York, NY, USA: McGraw-Hill, 2001.
[29] S. Yang, S. Liu, N. Zhang, G. Li, and J. Zhang, "A fully automatic-image-based approach to quantifying the geological strength index of underground rock mass," *Int. J. Rock Mech. Mining Sci.*, vol. 140, Apr. 2021, Art. no. 104585.

SEN YANG received the Ph.D. degree in mining engineering from China University of Mining and Technology, China, in 2019. He is currently a Lecturer with the School of Energy Science and Engineering, Xi'an University of Science and Technology. His research interests include rock mass remote sensing, mining automation, and rock damage acoustic characterization.

HONGRU LI received the B.Eng. degree in mining engineering from Luliang University, in 2019. He is currently pursuing the master's degree with the School of Energy Science and Engineering, Xi'an University of Science and Technology. His research interests include rock mass remote sensing and deep coal seam extraction.

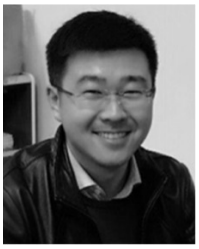

LI MA was born in Jixian, Shuangyashan, China, in 1986. He received the B.Eng. and Ph.D. degrees in mining engineering from China University of Mining and Technology, China, in 2010 and 2015, respectively.

From 2015 to 2017, he worked as a Postdoctoral Researcher with the State Key Laboratory for Geomechanics and Deep Underground Engineering, China University of Mining and Technology. He is currently working as an Associate Professor with Xi'an University of Science and Technology. He has authored more than 50 publications. He has ten years of research experience in the area of surface mining optimization.

WENYONG BAI received the B.Eng. degree in mining engineering from North China Institute of Science and Technology, Hebei, China, in 2013, and the M.S. degree in mining engineering from Xi'an University of Science and Technology, Shaanxi, China, in 2016, where he is currently pursuing the Ph.D. degree in mining engineering.

From 2016 to 2019, he was a Teaching Assistant with Shanxi Datong University. His research interests include overlying strata movement and mining-induced dynamic disaster.